Framework-Topology Controlled Singlet Fission in Metal-Organic Frameworks

Sreehari Surendran Rajasree,[†,a] Jierui Yu,[†,a] Fernando Fajardo-Rojas,[b] H. Christopher Fry,[c] Ryther Anderson,[b] Xinlin Li,[a] Wenqian Xu,[d] Jiaxin Duan,[e] Subhadip Goswami,[e] Karan Maindan,[a] Diego A. Gómez-Gualdrón,[b] and Pravas Deria*[, a]

[a] School of Chemical and Biomolecular Science, Southern Illinois University, 1245 Lincoln Drive, Carbondale, Illinois 62901, United States.

[b] Department of Chemical and Biological Engineering, Colorado School of Mines, 1500 Illinois St, Golden, Colorado 80401, United States.

[c] Center for Nanoscale Materials, Argonne National Laboratory, 9700 S Cass Ave, Lemont, Illinois 60439, United States.

[d] X-ray Science Division, Advanced Photon Source, Argonne National Laboratory, 9700 S Cass Ave, Lemont, Illinois 60439, United States.

[e] Department of Chemistry, Northwestern University, 2145 Sheridan Road, Evanston, Illinois 60208, United States.

ABSTRACT: Singlet fission (SF) has been explored as a viable route to improve photovoltaic performance by generating more excitons. Efficient SF is achieved through a high degree of interchromophoric coupling that facilitates electron super-exchange to generate triplet pairs. However, strongly coupled chromophores often form excimers, which can serve as an SF intermediate or a low-energy trap site. The succeeding decoherence process, however, requires an optimum electronic coupling to facilitate the isolated triplet production from the initially prepared correlated triplet pair. Conformational flexibility and dielectric modulation can provide means to tune the SF mechanism and efficiency by modulating the interchromophoric electronic interaction. Such a strategy cannot be easily adopted in densely stacked traditional organic solids. Here, we show that the assembly of the SF-active chromophores around well-defined pores of solution-stable metal—organic frameworks (MOFs) can be a great platform for a modular SF process. A series of three new MOFs, built out from 9,10-bis(ethynylenephenyl)anthracene-derived strut, show a topology-defined packing density and conformational flexibility of the anthracene core to dictate the SF mechanism. Various steady-state and transient spectroscopic data suggest that the initially prepared singlet population can prefer either an excimer-mediated SF or a direct SF (both through a virtual charge-transfer (CT) state). These solution-stable frameworks offer tunability of the dielectric environment to facilitate the SF process by stabilizing the CT state. Given that MOFs are a great platform for various photophysical and photochemical developments, generating a large population of long-lived triplets can expand their utilities in various photon energy conversion schemes.

INTRODUCTION

Singlet fission (SF) has become attractive pursuit as a potential performance booster in photovoltaics beyond the traditional Shockley-Queisser limit.[1, 2] Such exploitation, however, will critically depend on the high quantum-yield generation of usable triplets from the initially prepared triplet pairs, $^1(T_1T_1)$, through the SF process (eq 1).

$$[S_1S_0] \xrightarrow{k_{SF}} {}^1(T_1T_1) \xrightarrow{k_{decoh}} 2T_1 \qquad (1)$$

The k_{SF} of the spin-allowed SF process (i.e., the first step of eq 1) depends on the extent of electronic coupling between the initial singlet and correlated triplet pair states and is commonly described with the super-exchange electronic coupling term of $\langle S_1S_0|\hat{V}|T_1T_1\rangle$.[3-5] Therefore, the intuitive design of functional compositions would require an optimum electronic coupling between the molecular units (or subunits in the intramolecular process) –which should be strong enough to drive the first step but not so strong to suppress the decoherence. For traditional solid-state developments, crystal packing[6] (defining the π- π stacking and slip distances) dictates the extent of electronic couplings required for the SF process.[7] Such structural control, achieved via molecular side-chain engineering, can be a limiting factor for an efficient SF and decoherence of $^1(T_1T_1)$.[8] Intramolecular SF, developed in solvent-dissolved macromolecular systems, has identified several key design principles: for example, a through-bond electronic coupling,[9-11] the oligomer size providing a larger space,[12] and altering the extent of chemical conjugation through conformational modularity can tune both the SF and decoherence processes. Such strategies may not be adoptable in traditional solids.

Metal–organic frameworks (MOFs) have emerged as candidate materials in various energy conversion schemes. To maximize the photon energy conversion in such solid compositions, it is critical to comply with the general diffusion problem: efficient transportation of the excited energy (molecular excitons) to the catalytic sites and/or achieve long-lived excitons. The latter implies high quantum yield triplet generation, which is commonly achieved by using transition metal-based struts (e.g., $Ru(bpy)_3^{2+}$) with directly accessible MLCT triplets or via a triplet sensitization (using palladium-metallated porphyrins).[13-19] High quantum yield triplet generation in MOF can, alternatively, be achieved via SF as

the frameworks allow topology-dependent modular assembly of the SF-active struts (hereon denoted as P_{SF} for general purpose). The key factor, here, is the topology-defined pore geometry and assembly of the P_{SF} with appropriate strut-to-strut distance, orientation, and conformation for modular k_{SF} and decoherence process. Unlike traditional organic solid assemblies, solution-stable MOFs enable dielectric modulations tuning the SF efficiency and facilitating mass transport needed for energy conversion schemes. Therefore, SF in MOF can be envisioned to expand the applicability of the SF process, especially in solution-phase photochemical developments.

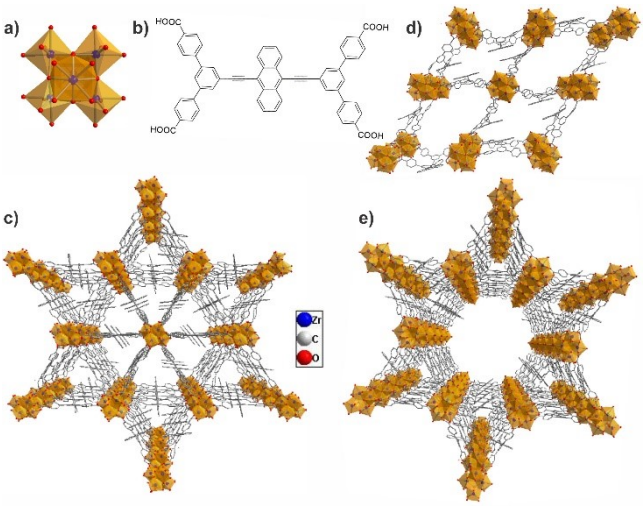

Figure 1. Structure of the a) Zr_6^{IV} −oxo node and (b) H_4PEA linker and their solvothermally-assembled frameworks (c) SIU-150, (d) SIU-152, and (e) SIU-175.

Complying with the requirement for a low-lying T_1 state (*i.e.*, $E_{S_1} \geq 2E_{T_1}$), 9,10-bis(ethynylenephenyl)anthracene -derived P_{SF} H_4PEA (= 5',5""-(anthracene-9,10-diylbis(ethyne-2,1-diyl))bis([1,1':3',1"-terphenyl]-4,4"-dicarboxylic acid) was prepared by hydrolyzing the corresponding Et_4PEA ester. To study the topological impact on the SF process, H_4PEA was assembled into three zirconium(IV) MOFs: SIU-150 (***ced***) and SIU-152 (***tty***), and SIU-175(***xly***) (Figure 1). Structural characterization of SIU-150 suggests that it adopts a distorted triangular packing assembly with [PEA] = 0.54 M, SIU-152 adopts a less dense diamond-shaped assembly with [PEA] = 0.37 M, whereas SIU-175 is a least dense assembly with [PEA]= 0.28 M arranged around triangular and hexagonal pores (see Table 1). All these frameworks satisfy the requirement to share its excited energy ($^1P_{SF}$*) with a neighboring strut fixed around the micropores of varying shape and content (per unit volume).

Various steady-state and time-resolved absorption and emission spectroscopic data suggest that SF, in these frameworks, involves a mechanism that is dictated by their topology-defined PEA assembly. In a densely packed SIU-150, the SF is mediated by an excimer-like complex as an intermediate, whereas in frameworks with lower PEA density, i.e., in SIU-175, a direct SF through the charge-transfer (CT) virtual state is preferred. The preference can be modulated by stabilizing the CT state by increasing the dielectrics of the environment. The compelling results presented here suggest that topological control of the SF mechanism in the solution-stable MOFs can be exploited as a platform to harvest in various energy schemes.

Experimental Section

Materials. Solvothermal assembly of the deprotonated H_4PEA linker with Zr_6-oxo node was achieved in N,N-dimethyl formamide (DMF; Fisher Sci.) or N,N-diethyl formamide (DEF; Sigma Aldrich) solvent. For this, $ZrOCl_2 \bullet 8H_2O$ (Sigma Aldrich) was treated with benzoic acid, 2,4,6-trimethylbenzoic acid, or a 1:1 mixture of benzoic acid and formic acid-based modulator at a specific temperature before assembling with H_4PEA. Detailed syntheses of the H_4PEA linker and the MOFs are given in Supporting Information (Section B). The synthesized MOFs were thoroughly washed with warm DMF and stored submerged under DMF. A portion of the synthesized MOF samples was exchanged with ethanol for supercritical CO_2 activation; these solids were used only to record nitrogen isotherms. The rest of the as-synthesized materials were thoroughly exchanged with 2-methyl tetrahydrofuran (MeTHF; Sigma-Aldrich), or α,α,α-Trifluorotoluene (CF_3Tol; Sigma-Aldrich) solvent before spectroscopic investigations. Samples for spectroscopic measurements were never dried of solvent to avoid any structural damage.

Instrumentation. Powder synchrotron radiation diffraction (PSRD) data were collected at beamline 17-BM of the Advanced Photon Source at Argonne National Laboratory. Solvent (DMF)-soaked MOF samples were loaded into Kapton capillaries (d= 1 mm). Diffraction data of these capillary-loaded samples were collected at the X-ray wavelength of 0.45256 Å using a VAREX XRD 4343CT flat panel detector. Diffused transmittance (T) spectra for MOF samples were measured using a JASCO V-670 UV-vis-NIR spectrophotometer outfitted with a 60 mm $BaSO_4$-coated integrating sphere. For this, MOF films (2 mg MOF, 20 mg polymethyl methacrylate in 1.5 mL chloroform) are made on quartz glass and were placed at the exterior entry point to reduce the scattering; the measured T was then converted to absorption using $I_{abs} = -log_{10}(T)$. This configuration provided absorption spectra with nominal scattering contribution. Steady-state excitation-emission spectra were collected using an Edinburgh FS5 spectrofluorometer in a front-face configuration, where samples, soaked in deaerated MeTHF or CF_3Tol solvent were packed in a Teflon-sealed quartz capillary tube.[20, 21] Absolute quantum yields (QY) were determined using a 150 mm integrating sphere. Time-resolved emission spectra and transient decay profiles of the bulk sample were recorded using an Edinburgh Lifespec II picosecond Time-Correlated Single-Photon Counting (TCSPC) spectrophotometer (λ_{ex} = 403 nm pulsed diode laser; pulse width = 60 ps, providing 160 ps IRF). Instrumental control, kinetic data collection, and processing were performed using F980 software. Femtosecond transient absorption spectroscopic data were collected on HELIOS Ultrafast Systems. Global target Analyses and time-resolved data fitting were performed using the Glotaran package.[22] The kinetic models used are described in SI (section F).

Computational Model. PSRD data were used for Rietveld refinement of computational MOF models to determine the MOF structures (see SI section C1). Computational models for SIU-150, SIU-152, and SIU-175 were built using the publicly accessible code ToBaCCo-3.0.[23, 24] The built models were optimized by minimizing the energy of the structure, where the dependence of energy on atom positions was provided by the Universal Force Field.[25] Then, the corresponding experimental PSRD patterns were used as the basis for Rietveld refinement (using Materials Studio-6.0)[26] of the models to elucidate the experimental lattice constants. Once these constants were found, atomic positions were reoptimized while keeping the lattice fixed. Slight adjustments of symmetry in the final MOF model were done "manually" using the Materials Studio-6.0 GUI. Simulated N_2 adsorption isotherms

at 77 K were obtained via grand canonical Monte Carlo (GCMC) simulations in RASPA-2.0,[27] in which temperature, volume, and chemical potential were kept constant (detail procedure is provided in SI section C2).

Vertical electronic excitations were computed via TDDFT method with small representative MOF models constructed from their crystallographic coordinates. In these computations, the metal-oxo nodes were removed and a proton was added to each carboxylate group to achieve charge neutrality in the model.[21] The model linker assemblies then underwent constrained optimization (HSE1PBE/6-311G(d,p)), where the terminal carboxylate atoms were fixed to their crystallographic coordinates, allowing the linkers to maintain their relative positions as defined by the respective framework topology. Oscillator strengths and their corresponding transition energies and densities were obtained *via* time-dependent DFT computation of 40 excited states on these DFT-optimized cluster models.

RESULTS

The H_4PEA linker was designed by appending 4-carboxyphenyl ligating arms to 9,10-bis(phenyleneethynyl)anthracene, a known SF-active chromophore.[7] Like the core, H_4PEA linker molecule does not show any detectible phosphorescence and satisfies the energetic requirements for singlet fission. TDDFT computation of H_4PEA at its most stable planer conformation provides $E_{S_1} \approx 2.43$ eV and $E_{T_1} \approx 1.18$ eV, where the strong, lowest energy, x-polarized transition dipole lies along its long molecular axis.[28] In contrast, a relatively weak higher-energy y-polarized transition dipole is aligned along the long anthracene axis. The low torsional energy barrier also implies a wide range of thermally accessible torsional populations (see SI sec D1) to broaden its spectral envelope.

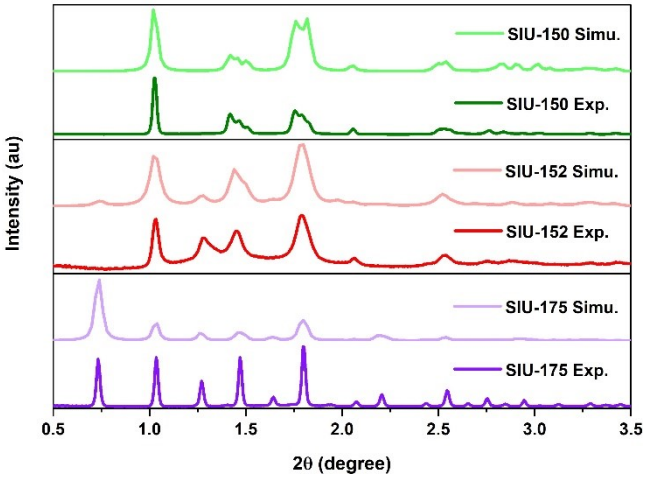

Figure 2 PSRD patterns collected for DMF-soaked SIU-150 (*yellow*) and SIU-152 (red). The simulated pattern of SIU-150 (*green*) and SIU-152 (*orange*) obtained from Rietveld modeling and QPA showed good agreement with the experimental patterns.

To study the impact of topology-defined arrangement on singlet fission, H_4PEA was assembled into three structurally different but chemically comparable MOFs. SIU-150 was obtained as small hexagonal button-shaped crystals (Figure S3a); an anisotropic variant can be obtained under the synthetic condition that promotes slower growth (Figure S3b). SIU-152, on the other hand, is formed under a kinetically controlled condition at a low temperature that gives rise to 100-300 nm size spindle-shaped crystallites (Figure S3d). SIU-175 was prepared under more thermodynamically controlled conditions at higher temperatures and formed needle-like crystals (Figure S3c). Rietveld fitting of powder synchrotron diffraction (PSRD) data (Figure 2) suggests that the SIU-150 is based on a ***ced*** net, SIU-152 was assembled with a ***tty*** topology, and SIU-175 is constructed on ***xly*** net.[29]

Congruent with the framework structural features and behaviors established for flexible linkers,[30] like those with elongated aromatic backbones,[31] SIU-150, SIU-152, and SIU-175 underwent capillary-force-driven pore-shrinkage and, therefore, significant structural collapse occurs upon removal of the occupied solvents -even during a mild supercritical CO_2 (SCO) activation process (Figure S3e-g). Measured N_2 isotherms recorded for these SCO-activated samples (at 77 K; Figure S6) display Type-II isotherms with low surface area values: SIU-150: 240 m^2g^{-1}, SIU-152: 500 m^2g^{-1}, and SIU-175: 200 m^2g^{-1}. These values indicated that SIU-175, with mesopores, undergoes severe structural collapse (Figure S6). The experimental pore size distribution, extracted from the measured N_2 isotherms, matches well with the computationally predicted pore size patterns: these data suggest that the pore collapse is not completely global – some residual 'undamaged' regions report porosity (and part of the surface area). To ensure that these frameworks are indeed low-density porous compositions, solvent-accessible porosity was probed via thermogravimetric analysis (TGA) of the respective DMF-filled MOF samples. All the MOF samples showed an initial mass loss of $\gtrsim$ 90% (i.e., associated with the evaporation of the solvent filled within the MOF pores) –indicating high gravimetric porosity (see SI sec C3).[32] For all our spectroscopic investigations, however, all the MOF samples were stored (and handled) submerged in desired solvents without ever evacuating them[33] to ensure that the photophysical properties correspond to their open structures as determined from the diffraction data.

Table 1. The concentration of PEA Linker in SIU-150, SIU-152, and SIU-175.

MOF	Unit cell dimension (Å^3)	Unit cell volume (L)	# of PEA /unit cell	[PEA] (M)
SIU-150	42.4×40.9×25.3	3.679×10^{-23}	12	0.54
SIU-152	41.6×40.1×25.2	3.629×10^{-23}	8	0.37
SIU-175	40.1×40.6×25.1	3.586×10^{-23}	6	0.28

These [PEA] values are comparable to the relevant structure.[34]

To understand how the PEA linker arrangements within these frameworks (Figure 1) impact their photophysical properties, their packing density as a function of their topology was examined: the linker concentration [PEA] in these structures was determined from the number of linkers present in the unit cell (Table 1). SIU-150 arranges PEA linkers most densely around triangular micropores and the structure propagates on the *ab*-plane by sharing the edge. In contrast, SIU-152 arranges PEA linkers in a slightly less dense fashion around edge-sharing rhombic pores, and the least dense SIU-175 framework is constructed by propagating the triangular arrangement in a node-sharing manner (i.e., around hexagonal mesoporous channel). These basic differences in the PEA arrangement are expected to dictate different inter-linker distances (*i.e.*, PEA—PEA) and therefore, electronic interaction determining their spectral evolutions[34, 35] and excited-state dynamics including the SF process. Crystallographic data suggest that the anthracene moieties in these frameworks, can have a rotational degree of freedom, and the extent will be determined by their framework assembly that dictates the extent of a steric hindrance as well as the strain on the Ph-C≡C-Anth-C≡C-Ph axis expressed by the network. Nonetheless, the TDDFT results with small representative model arrays suggest $E_{S_1} \geq 2E_{T_1}$ (*vide infra*).

The extent of the inter-linker electronic interaction as a function of topological arrangement can be seen in their absorption spectra

(Figure 3). Compared to the solution-dissolved linkers, all the MOFs displayed some degree of redshift for their low-energy transitions. For example, the low energy transition for the solution-dissolved linkers peaks at ~455 nm; all the MOF samples display a corresponding transition at 474 nm. Overall spectral envelopes for all the MOFs are comparable except that the relative oscillator strength for the 475 nm peak is higher in SIU-152, whereas the shoulder at 500 nm is more apparent for the other two. This is stemming from different torsional population and their respective exciton splitting (Figure S9). To understand this point, a small model was constructed with three PEA linkers as assembled in their framework: a triangular array was constructed from the SIU-150 crystallographic coordinates and a zigzag array from the SIU-152. Each of these initial structures was systematically optimized, where the large band-gap zirconium-oxo clusters were omitted for simplicity, and the protonated carboxylates were fixed in their crystallographic positions (Figure 3c and d).[21, 31, 36] Simulated absorption spectra (Figure 3b) generated from the respective TDDFT computed transition energies and oscillator strengths for these optimized models matched well with the experimental spectra (Figure 3a). These data highlight the relative orientation of the PEA linkers and the anthracene torsional angles (see Figure S9) define the absorptive spectral evolution.

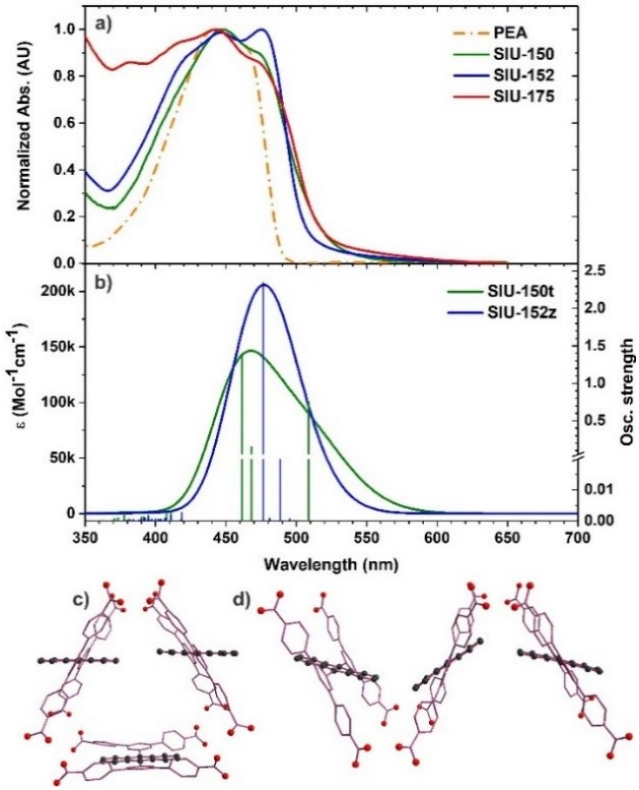

Figure 3. Absorptive electronic transitions of the MOFs: (a) the experimental spectra of SIU-150 (green), SIU-152 (blue), and SIU-175 (red) along with the linkers H_4PEA linker (dashed, dark yellow). (b) the TDDFT computed absorption spectra of small MOF models—shown in panel (c) for SIU-150 and (d) for SIU-152; (absorption spectra were simulated via a Gaussian reconvolution (FWHM = 2500 cm^{-1}) of the TDDFT computed oscillator strengths).

Steady-state emission spectroscopy. Steady-state excitation-emission mapping spectra (EEMS) for the Et_4PEA and MOF samples were collected in MeTHF solvent and presented in Figure 4. The EEMS plot for Et_4PEA (Figure 4a) highlights two excitation/emission manifolds. The lowest energy manifold, involving an S_1 excitation and $S_1 \longrightarrow S_0$ emission, is centered at 450/482–550 nm (Φ_{em} ~ 98%) with well-resolved vibronic structures appearing at 482 ($\upsilon_{0\text{-}0}$), 515 ($\upsilon_{0\text{-}1}$), and 545 ($\upsilon_{0\text{-}2}$) nm. The higher energy manifold, *i.e.*, an S_2 excitation and $S_1 \longrightarrow S_0$ emission, is centered at 275-315/482-550 nm. Congruent with the literature report established for the core pigment 9,10-bis(ethynylenephenyl)anthracene, the protonated H_4PEA or the ester-protected Et_4PEA did not display any detectible phosphorescence even for the later in frozen glassy MeTHF –this indicates a poor singlet-to-triplet intersystem crossing; $\Phi_{ISC} \lesssim 10^{-5}$-$10^{-4}$).[37]

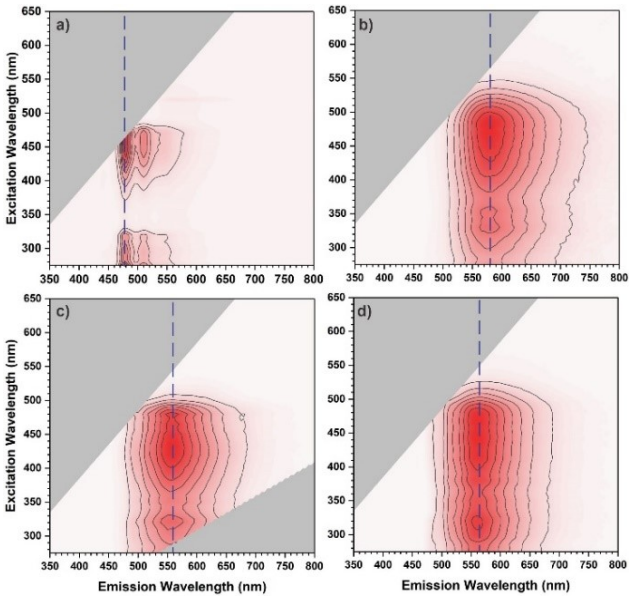

Figure 4. EEMS plots of (a) Et_4PEA (~*ca* 0.4 μM), b) SIU-150, c) SIU-152, and (d) SIU-175 collected in deaerated MeTHF solvent (T = 298 K; color code: dark red being the most intense).

In contrast, the EEMS plot for SIU-150 highlights its lowest energy excitation/emission manifold with a broad maximum around 475/580 nm (FWHM ~3390 cm^{-1}; Figure 4b) that extends well beyond 750 nm with an overall Φ_{em} ~ 11%. For SIU-152, the combined EEM manifold peaks around 430/560 nm (FWHM ~ 3468 cm^{-1}) with an overall Φ_{em} ~ 36%. Likewise, the EEM manifold recorded for SIU-175 peaks around 475/565 nm (FWHM ~ 3203 cm^{-1}) –with an overall Φ_{em} ~ 39%. In general, the broad spectral linewidth can be associated with excimer-like complex (S_{exc}) formation giving rise to unresolved $S_1 \longrightarrow S_0$ and $S_{exc} \longrightarrow S_0$ lines[34] or a low-energy delayed fluorescence stemming from triplets-triplet annihilation (TTA). Signature of an excimer-like complex formed in a closely packed TBAPy- MOF, NU-901 (with [TBAPy] = 0.65 M; TBAPy =1,3,6,8-tetrakis(*p*-benzoicacid)pyrene) rendered a broad emission profile with FWHM ≈ 3400 cm^{-1} where a larger pore NU-1000 (with [TBAPy] = 0.41 M; leading to a less extent and weaker excimer formation) entailed a narrower emission envelop (FWHM ≈ 2660 cm^{-1}).[34] Nonetheless, in these PEA-MOFs, the formation of broad low-energy emission spectral envelop can be better understood from the time-resolved spectra.

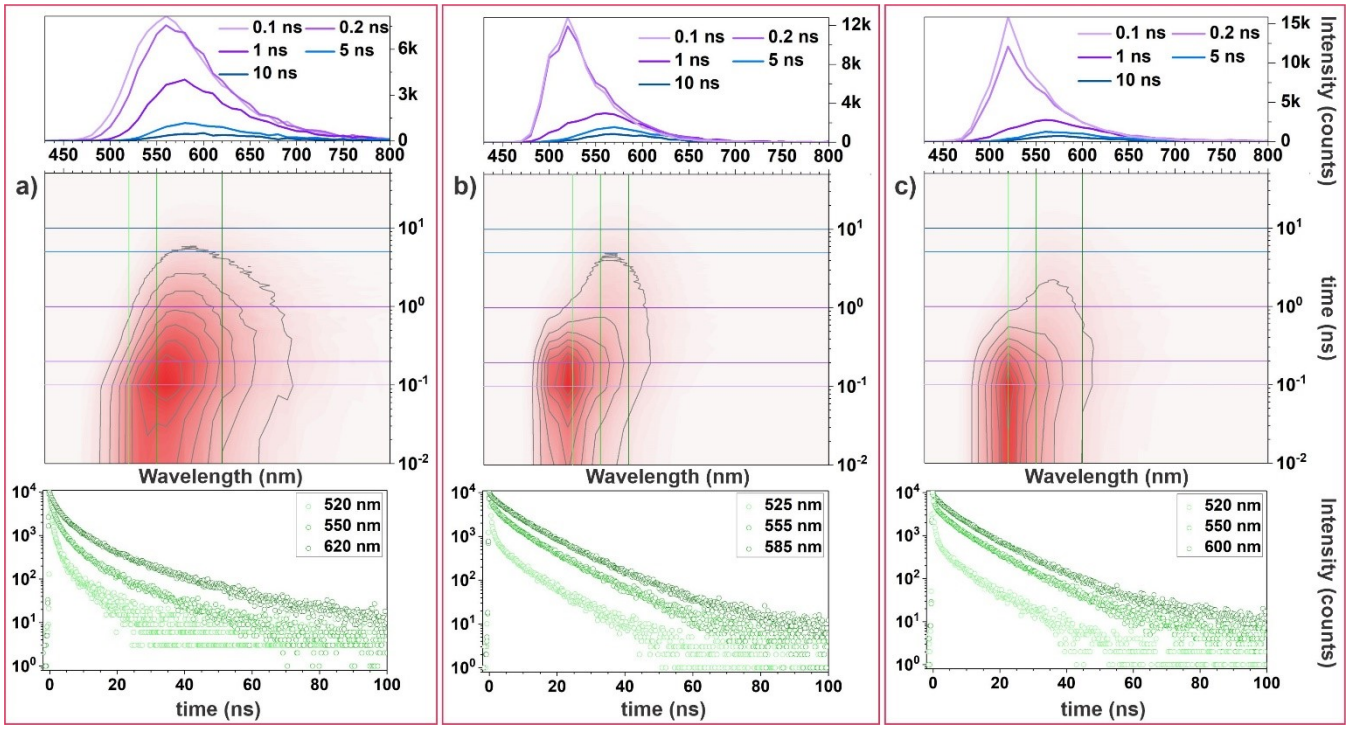

Figure 5. TRES data plotted for the MOF samples in MeTHF solvent (λ_{ex} = 403 nm; 298 K). The contour plots for samples (a) SIU-150, (b) SIU-152, and (c) SIU-175 show the time evolution of the spectra with intensity. The respective transient emission spectra at labeled time delays are shown at the top panels and representative transient kinetic profiles probed at labeled wavelengths are presented at the lower panels.

Time-resolved emission spectra. The evolution dynamics of the emissive species were probed via time-resolved emission spectra (TRES) by analyzing corresponding transient emissive profiles: data collected in MeTHF solvent are presented in Figure 5. As seen in the steady-state EEMS, the TRES plot for SIU-150 displays a broad spectral envelope peaking at 560 nm at an early time (~0.05 ns) and maintained its broad linewidth (FWHM = 3050 cm^{-1} measured at 0.1 and 1 ns; Figure 5a top panel) as the peak steadily shifts to 580 nm over time. In contrast, SIU-152 starts with a narrow emission line (FWHM = 1930 cm^{-1}) peaking at 525 nm at 0.05-0.1 ns, where a broad absorption band, peaking at ca 570, appears ~ 1 ns (FWHM = 3030 cm^{-1}) and dominate the spectral envelop thereon.

Likewise, SIU-175 produces narrow spectra at the earlier time (FWHM = 1750 cm^{-1} measured at 0.05-0.1 ns) peaking at 525 nm, and a broad band centered at ca 575 nm appears late (FWHM = 3250 cm^{-1} measured at 1 ns). The TRES data suggest possible origins for the broad steady-state emissive spectral lines: an unresolved $S_{exc} \longrightarrow S_0$ in SIU-150 that started from the early stage, whereas, in SIU-152 and SIU-175, a delayed formation indicates the involvement of TTA. Involvement of TTA in SIU-150 can be viewed from the steady redshift of the initial broad emission line to 580 nm over time (like the other two MOFs) from the broad ~550 nm line (for $S_{exc} \longrightarrow S_0$; *vide infra*). Global fitting of the transient kinetic profiles suggests that the emissive spectral envelope has three time constants (Table 2): a fast τ_1 ~ 0.25 (± 0.05) ns component can be assigned to the inherent $S_1 \longrightarrow S_0$ emission, which is significantly shorter than the solution-dissolved Et_4PEA linker (2.56 ns). The longer time constants (τ_2 and τ_3 in nanosecond timescale) can be assigned to the $S_{exc} \longrightarrow S_0$ and delayed emission. A relatively shorter τ_2 for SIU-150 may indicate that S_{exc} is an intermediate to populate other excited states, and the delayed emission could well be from a low energy emissive state (denoted as S_ℓ) that is reverse-populated by TTA (Table 2; see quenching experiments, *vide infra*) and, therefore, should depend on the triplet population [T_1].

The existence of multiple emissive species was further verified by analyses of the wavelength-dependent transient profiles: the kinetic profiles probed at the blue side of the emissive envelope (*e.g.*, at 525 nm) decay faster compared to the kinetic profiles probed at the red side (Figure 5 lower panels). To understand the nature of the excited states (intermediates) involved in the delayed S_ℓ formation, we probed the TRES data in CF_3Tol solvent (Figure S13). Generally, narrower spectral envelops were observed in CF_3Tol solvent compared to those recorded in MeTHF solvent. The TRES plot for SIU-150 begins with a broad spectral envelop peaking at 525 nm (FWHM = 2423 cm^{-1} measured at 0.05-0.1 ns) and the peak broadens (FWHM = 3730 cm^{-1} measured at 1 ns) as it steadily shifts to 580 nm over time (Figure S13). The narrower bandwidth in polar solvents helps resolve various emission bands. For SIU-175, the $S_\ell \longrightarrow S_0$ envelope is significantly narrow (FWHM = 2085 cm^{-1} measured at 1 ns) and decays quickly. Global fitting of the kinetic profiles suggests that the τ_1 [~ 0.25 (± 0.05) ns] is not solvent polarity dependent, whereas the longer (τ_2 and τ_3) time constants are significantly shortened for SIU-152 and SIU-175 in CF_3Tol solvent (see Discussions).

Table 2. Emission Lifetime Data for Et_4PEA and the MOF Samples

Compound	Solvent (ε)	Φem	τ_1 (ns)	τ_2 (ns)	τ_3 (ns)
Et_4PEA	MeTHF (6.97)	98%[c]	2.56	-	-
	CF_3Tol (9.18)		2.47		
SIU-150	MeTHF (6.97)	11% (8%)[a]	0.21	1.7	9.1

	CF_3Tol (9.18)	9%	0.21	1.1	7.2
SIU-152	MeTHF (6.97)	36% (29%)[a]	0.28	3.8	12.5
	CF_3Tol (9.18)	27%[c]	0.23	1.0	7.6
SIU-175	MeTHF (6.97)	39% (17%)[a]	0.25	3.0	11.3
	CF_3Tol (9.18)	23%[a]	0.30	1.0	7.3

Data collected at RT, argon; error manifested in time constants ± 0.05 ns. [a] measured in air purged media.

Transient Absorption Spectroscopy. Femtosecond transient absorption (fs-TA) spectra of Et_4PEA (λ_{ex} = 450 nm; MeTHF; 298K) represent a single species (Figure S14) highlighted by a broad but intense excited-state absorption (ESA) band for $S_1 \longrightarrow S_n$ transitions at 530-750 nm, ground-state bleaching (GSB) at 460 nm, and stimulated emission (SE) at ~515 nm without any triplet feature (through SF or ISC). The S_1 species had a lifetime τ = 2.26 ns, like that obtained from the TRES data (Table 2).

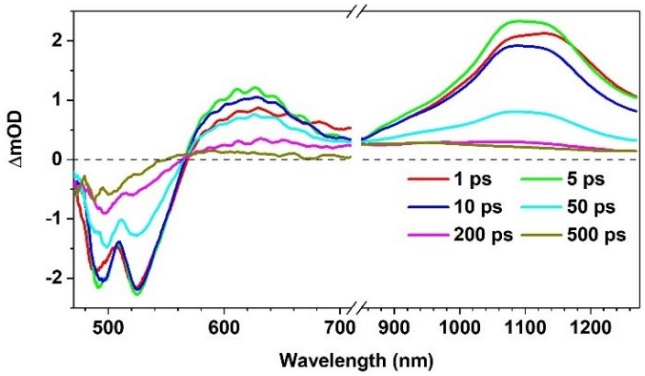

Figure 6. Representative fs-TA spectra for SIU-152 suspension in MeTHF solvent at labeled delay times. Experimental condition: λ_{ex} = 390 nm; fluence= ~600 μJ/cm^2.

The fs-TA spectra for all three MOFs samples (λ_{ex} = 390-430 nm, MeTHF, 298K; Figures 6, S15-S18) highlight the evolution of multiple transient species as a function of their structure. Generally, at early times, the ESA bands, one peaking at *ca* 640 nm and the other intense broad one at *ca* 1150 nm, for $S_1 \longrightarrow S_n$ transitions can be seen along with the GSB at 480-500 nm and a SE at ca 525 nm. Based on the singular value decomposition (SVD) analyses, the fs-TA spectral data (wavelength-intensity-time) were globally fit with a three- or two-species sequential target model (i.e., [**A** →(k_1)→ **B** →(k_2)→ **C** →(k_3)→ gs; or [**A** →(k_1)→ **C** →(k_3)→ gs]; Figure 7).

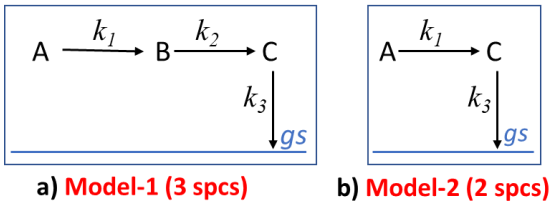

Figure 7. Adopted GTA models: a) a three-species model-1, and (b) a two-species model-2.

Confidentiality of the fit (*i.e.*, a two vs three species model or a branched model) was assessed from the error against the experimental data (See SI sec F; Figures S19-24).[38] In general, the initial singlet species **A** (a singlet pair, S_1S_0) decays to species **B** (an SF intermediate) with k_1. Likewise, species **B** decays to species **C** with k_2. In the fs-TA instrumental timescale, intermediate **C** can be triplet and its dynamics can only be probed until *ca* 10 ns. The kinetic process involved in these GTA models:

$$\frac{d[A]}{dt} = -k_1[A] \qquad (2)$$

$$\frac{d[B]}{dt} = k_1[A] - k_2[B] \qquad (3)$$

$$\frac{d[C]}{dt} = k_2[B] - k_3[C] \qquad (4)$$

For the two-species GTA (model 2), [B] term is nonexistence. The fs-TA data collected for SIU-150 (in MeTHF solvent; Figure S15a) fit best with three-species GTA model-1; the resulting species-associated spectra (SAS) are presented in Figure 8a (top panel). For this sample, the initial singlet species **A** (red SAS, with a GSB at 500 nm and a ~525 nm shoulder for SE), decays to species $\mathbf{B}_{150}$ with k_1 = (10 ps)$^{-1}$. The spectral signature of $\mathbf{B}_{150}$ (green SAS; Figure 8a) is highlighted by a broad ESA spanning 550-1300 nm that reminiscences to the TA-spectral features of S_{exc} reported for a

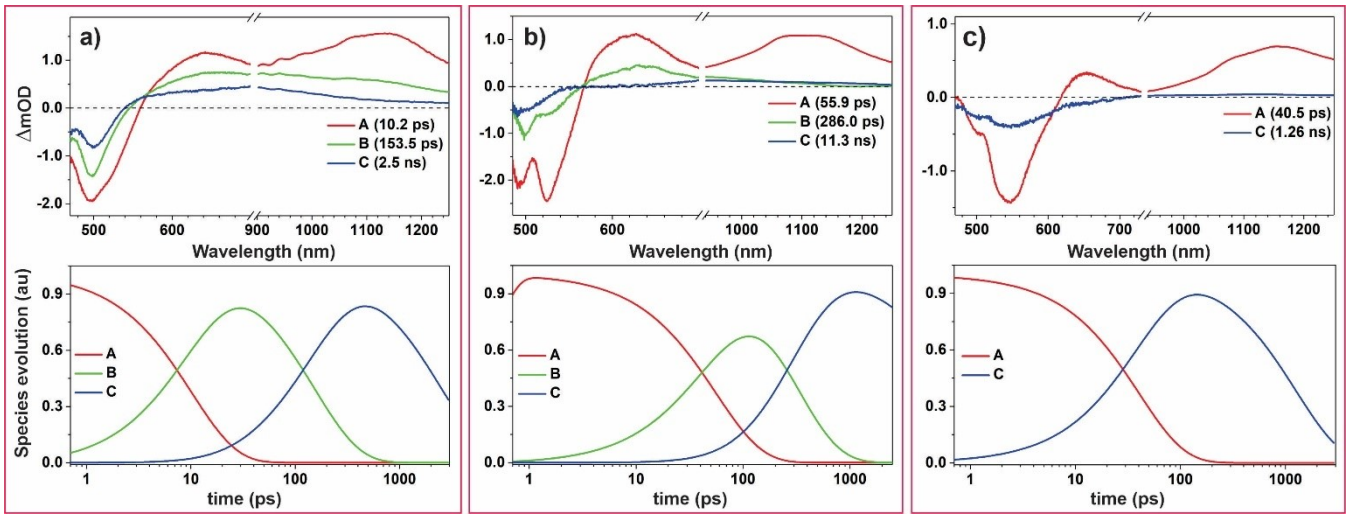

Figure 8. Plots of SAS generated from GTA model fit of the fs-TA data for (a) SIU-150, (b) SIU-152, and (c) SIU-175 in MeTHF solvent. Corresponding population dynamics are shown in the lower panels. See Figures S15-S18 for the fs-TA spectra at a different time delay.

related TBAPy-MOF.[21, 34] Thus, species $\mathbf{B}_{150}$ can be assigned to S_{exc}, and it decays to species $\mathbf{C}_{150}$ with $k_2 = (154\ ps)^{-1}$. Species $\mathbf{C}_{150}$ (blue SAS) decays with $k_3 = (2.5\ ns)^{-1}$ decay rate. Population dynamics of these species (Figure 8a bottom panel) suggest *ca* 85% of the initial singlet population forms species $\mathbf{C}_{150}$, considering no other non-radiative decay.

Similarly, the three-species (model-1) fit of the fs-TA data collected for SIU-152 rendered the initial singlet species $\mathbf{A}_{152}$ (red SAS; Figure 8b) with a GSB at ~480 nm along with an SE at 525 nm. It decays to species $\mathbf{B}_{152}$ with $k_1 = (56\ ps)^{-1}$. The spectral signature of species $\mathbf{B}_{152}$ is similar to that is $\mathbf{B}_{150}$ except for the broad ESA band expanding to 1300 nm. It decays to $\mathbf{C}_{152}$ with a $k_2 = (286\ ps)^{-1}$. Analysis of the respective population dynamics suggests that ~80% of the initial singlet population ($\mathbf{A}_{152}$) forms species $\mathbf{C}_{152}$, which decays with $k_3 = (11.3\ ns)^{-1}$. In contrast, the fs-TA data collected for SIU-175 can be best fit with a two-species GTA model-2 (Figure 7b). The initial singlet species $\mathbf{A}_{175}$ (red SAS; Figure 8c) appears to have a GSB at ~500 nm along with an intense SE at 550 nm. It decays to species $\mathbf{C}_{175}$ with $k_1 = (41\ ps)^{-1}$. Species $\mathbf{C}_{175}$ (blue SAS; Figure 8c) has a lifetime of $\tau = 1.2$ ns, and population dynamics suggest that ~ 90% of the initial $\mathbf{A}_{175}$ forms $\mathbf{C}_{175}$. Decay of the species **C**, for all these MOFs, was corroborated *via* the ns-TA experiment (Figure S15b), which consistently displayed a broad, long-lived, and featureless spectral signature.[39]

DISCUSSIONS

Characterization of the triplets: To assign the unique SAS plots, generated via these GTA model fits, the triplet state was probed. For this, triplet quenching experiments were first carried out to realize the existence of the triplet states. As discussed before and summarized in Table 2, O_2 quenching experiments suggest a sizable reduction of the delayed emission from S_ℓ state populated via TTA (Figure S27). The corresponding ns-TA data suggest the quenching of the signal from early (<10 ns) evolved species **C** (Figure S28; nonetheless, the ns-TA data provides unresolved earlier singlets –due to the instrumental detection limit).

Triplet characteristics of species **C** were further probed via a quenching experiment without involving any $^1O_2$ (that can form anthracene endoperoxide) or radical formed via a photo-induced redox reaction. For this, *all-trans*-retinoic acid (*at*RA) was installed at the SIU-175 forming *at*RA@SIU-175 (See SI sec G1.b). Energetically, *at*RA possesses a higher singlet and low triplet relative to the PEA linkers or its assemblies (Figure S29) -ensuring a perfect triplet quencher that can be anchored at the Zr-oxo node through its carboxy appended group exploiting SALI chemistry (Scheme S2).[20, 40-43] Compared to the pristine SIU-175 (QY = 39%), the *at*RA@SIU-175 (QY = 14%) displayed an emission quenching of the TTA-manifested singlets (Figure S30) with an extent that is better than molecular O_2 (QY = 17%). The ns-TA kinetic data of this sample displayed a similar quenching behavior of the early-time component (Figure S30c).

With these quenching experiments of the triplets, it was important to determine the TA signature of the triplets. For this, carboxy-appended palladium porphyrin sensitizer TCPP(Pd) (= tetra-(carboxyphenyl)porphinato palladium (II); see SI sec G2) was installed at the Zr-node. The TCPP(Pd) sensitized ns-TA ($\lambda_{ex} = 532$ nm; red to PEA absorption) data were used to generate 'synthesized' triplet spectra by subtracting a scaled TCPP(Pd) ns-TA spectrum (Figure S32). These synthesized triplet spectra are reminiscent of the spectral signature of respective species **C** (Figure S32). Technical differences related to triplet generation via a high-energy singlet vs a low-energy triplet sensitized method (coupled with instrumental limit and scattering) lead to some discrepancies: these include some unresolved singlet features (e.g., the tail of SE ~525 nm and broad ESA >600 nm) in the SAS of species **C** generated from TA data collected for the pristine MOF at the 355 nm excitation (Figures S15b, S16b, and S25a,b). These sensitized experiments also showed that the triplet spectral signature of these MOFs appears roughly in the same wavelength range of their steady-state absorption bands and can be dominated by the GSB.[7, 8]

Mechanism: Excimer (S_{exc}) –mediated SF pathway[4] has been sketched out within the context of the electron super-exchange process[44] that involves a CT virtual state. Considered as a possible trapped state,[45-47] S_{exc} can serve as an intermediate for triplet pair formation.[4, 48] The S_{exc} state can be described as $|S_{exc}\rangle = C_1|^1P_A^*\ P_B\rangle + C_2|P_A\ ^1P_B^*\rangle + C_3|P_A^+\ P_B^-\rangle + C_4|P_A^-\ P_B^+\rangle$; where C_n is the coefficients, and P_A and P_B are the two adjacent pigments –with small variable CT contribution (i.e., $C_3|P_A^+\ P_B^-\rangle + C_4|P_A^-\ P_B^+\rangle$) depending on the molecular constituents and their arrangements.[4] Nevertheless, these low-energy S_{exc} can generate $^1(T_1T_1)$ going through the CT state (Figure 9).

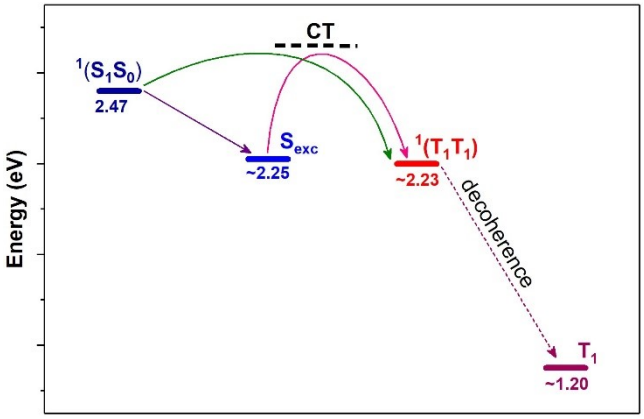

Figure 9. The evolution of the excited-state species involved in the SF process. The energy of the singlet, excimer, and triplet states was approximated from the $E_{0,0}$ and emission data along with the computational values.

Species **A**, with a spectral signature similar to the linker singlet (Figure S14; vide supra), was assigned to an initial singlet pair S_1S_0 (with neighboring *gs*-chromophore within the assembly). In low polar solvent, this starting pair, depending on the packing density, can form a low-energy S_{exc}.[21, 34] MOFs with lower density, which will render a lower probability to form such low-energy complexes. In other words, with a small C_1 and C_2 such systems will facilitate the CT contribution. Thus, in SIU-150, **C** formation is preceded by an efficient **B** formation ($k_1 \sim (10\ ps)^{-1}$), where **B** to **C** formation is the rate-limiting step ($k_2 \sim (150\ ps)^{-1}$). In contrast, SIU-175 efficiently forms **C** ($k_1 = (40\ ps)^{-1}$) without any low-energy intermediate (e.g., **B**). Therefore, species **B** is a key intermediate for SIU-150 and can be assigned to S_{exc} -due to the similarity of its broad ESA spanning 550-1300 nm with that of S_{exc} reported for a related TBAPy-MOF.[21, 34] And in this MOF, the spectral signature of **C** (from fs-TA data) remained somewhat unresolved from this stable S_{exc} contribution. In contrast, the spectral signature for $\mathbf{B}_{152}$ (green SAS; Figure 8b) lacks the broad ESA band expanding to 1300 nm -indicating a suppressed formation of S_{exc}. The fs-TA data and the SAS for SIU-175 (Figure S18; Figure 8c) in MeTHF solvent display an intriguing signature for $\mathbf{A}_{175}$: a broad, well-resolved (from the GSB) SE at *ca* 550 nm appearing as early as <1 ps. Given that TRES data (Figure 5c) suggest that a SE (from the initial singlet) should appear, like SIU-152, at ~525 nm –the 550 nm SE is therefore, assigned to the SE from the $^1(T_1T_1)$ pair. A low [PEA] in SIU-175 also does not support

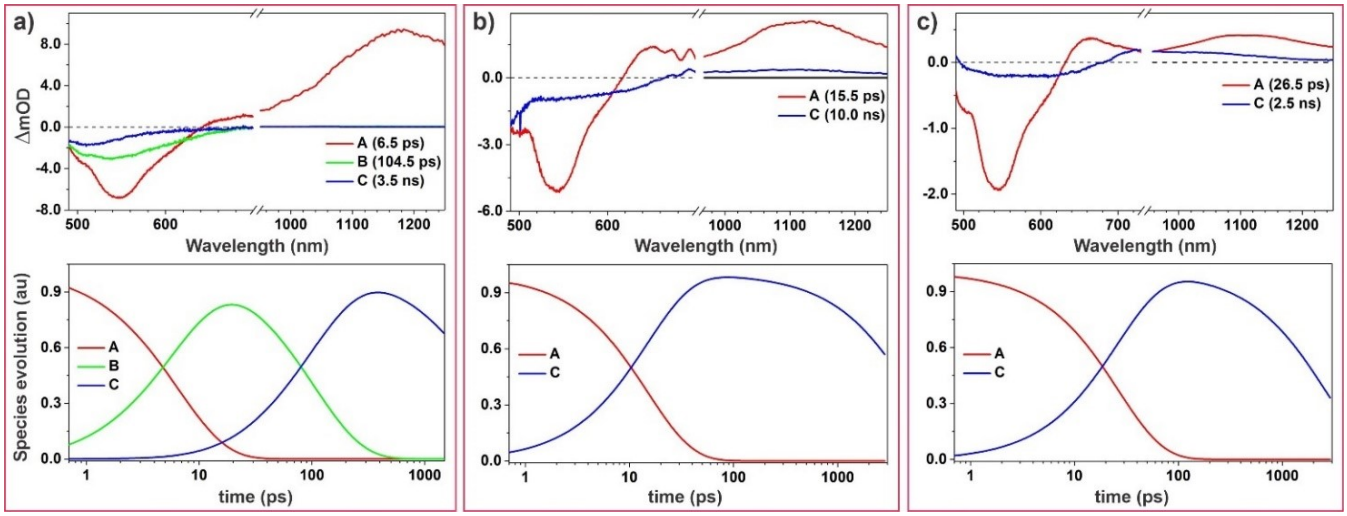

Figure 10. Plots of SAS obtained through GTA (model-1 or model-2; Figure 7a,b) fit of the fs-TA data for (a) SIU-150, (b) SIU-152, and (c) SIU-175 recorded in CF_3Tol solvent. Corresponding population dynamics are shown in the lower panels. See Figures S15-S18 for the fs-TA spectra at different time delays.

such a low-energy singlet emission (relative to the other two MOFs), and at this early time delay this 550 nm feature is not expected to appear from TTA populated S_ℓ. The fast appearance of this feature indicates an efficient SF process in SIU-175 without the involvement of a S_{exc} intermediate. This assignment can be further supported by the transient data collected in a higher dielectric medium (in CF_3Tol solvent, *vide infra*; Figure 10).

A low dielectric environment in densely packed organic chromophore assemblies can lead to a destabilized CT state, and therefore, facilitates to formation S_{exc} first. In such systems, modulation of the CT state energy (and contribution) can be a way to influence the underlying SF process. In our densely packed SIU-150, the SF proceeded through the S_{exc} formation. With a lower [PEA] in SIU-152 and further in SIU-175, the S_{exc} formation was low, and a direct $^1(T_1T_1)$ formation was observed.[49] Unlike traditional solid-state chromophore assemblies, these solution-stable MOFs allow dielectric modulation by simply infiltrating the pores with the desired solvent. TRES data collected for SIU-150 in polar CF_3Tol solvent (ϵ = 9.2) evinced even faster decay of these S_{exc} including a reduction in the spectral linewidth (FWHM = 2420 cm^{-1}; Figure S13) at the early stage. As summarized in Table 2, generally, Φ_{em} is lowered in polar solvent corroborating with the faster τ_2 and τ_3. These data suggest the involvement of the polar/CT state for the lower-energy emissions and that the dielectric of the environment can modulate the triplet pair formation route from a S_{exc}-mediated process to a direct CT-mediated path.

The fs-TA data collected in polar CF_3Tol solvent were similarly fit according to SVD analyses (*vide supra*; SI sec F2), the SAS and population dynamics are summarized in Figure 10. Congruent with the above assignments of the species involved in the SF pathways, all the samples consistently showed similar SAS for species **A** which is highlighted by a prominent SE at 550 nm. Although SIU-150 was fit with the 3-species model-1 (Figure S22), the SAS of species **B**, in CF_3Tol solvent, lacks the broad ESA signature of S_{exc}. An efficient direct CT-based $^1(T_1T_1)$ formation can also be viewed from the SE at 550 nm, unresolved with the initial singlets, in all the MOF samples (Figure 10; SAS of **A**). The extent of favorable CT-based SF in SIU-152 is such that a two-species model-2 can sufficiently fit (Figure S23) the corresponding fs-TA data with k_2 = (16 ps)$^{-1}$. In contrast, SIU-175 did not show a significant difference in CF_3Tol solvent, except the triplet forms more efficiently k_1 = (26 ps)$^{-1}$ compared to that was observed in MeTHF solvent (k_2 = (40 ps)$^{-1}$). Overall, the ns-TA data recorded in CF_3Tol solvents corroborates the lifetime of species **C** (Figure S26).

The TTA process is well-known to repopulate high-energy singlets.[16-19, 50, 51] This process will depend on the triplet population [T_1] and their diffusion to collide with each other. The latter will be more pronounced in closely packed assemblies facilitating a Dexter-like triplet migration.[16, 19] Examining the extent of the low-energy emission quenched by O_2, we can conclude that SIU-175 produces the largest quantity of the triplet than SIU-152 and SIU-150 –despite SIU-175 consists of the least [PEA] –which indicates that a high triplet population must be involved in it. To further probe if the low-energy quenchable delayed emission is resulting through TTA, sensitized emission spectra were collected for the palladium porphyrin-modified SIU-175 sample (Figure S31). A 480 nm (PEA-centered) excitation of this sample yielded three well-resolved bands at 510, 550, and 580 nm (this profile is like that of the atRA@SIU-175 sample for which the 580 nm band was unresolved; Figure S30). In contrast, a selective porphyrin excitation at 528 nm yielded 580 nm emission without much of the 550 nm band. These data also suggest that the low-energy delayed emission (580 nm) appears from the TTA-populated state that is different from S_{exc} state (Figure 5a). Based on the extent of this delayed emission quenching by molecular oxygen, an expected relative triplet population would be SIU-175 > SIU-152 > SIU-150.

CONCLUSION

This study—with three topologically different MOFs constructed from 9,10-bis(phenyleneethyne)anthracene (PEA) derived strut—has shown that the singlet fission (SF) process and its underlying mechanistic path can be dictated by the topology and pore geometry of the framework. Complying with the key requirements for SF, the 4-carboxyphenyl appended PEA strut was designed and assembled in three frameworks, SIU-150, SIU-152, and SIU-175, with lowering PEA packing density across the series. All these frameworks possess 1D pore channels along their *c*-axis, which enables a parallel PEA arrangement with different geometry and packing. Unlike traditional organic solids, the MOF pores can facilitate dielectric modulation as well as provide conformational flexibility for beneficial future development. The initially created

singlet populations can undergo SF through the virtual CT state or can first form a S_{exc} intermediate that then proceeds to SF through CT. In SIU-150, a densely arranged PEA around the triangular pore facilitates an excimer-like complex (S_{exc}) formation in a low-dielectric medium. In contrast, for SIU-152 and SIU-175, with a lesser density of the PEA assemblies, a direct CT-based SF was preferred. A switch in the SF mechanism (preference of direct CT vs S_{exc} -mediated) was realized by infiltrating the pores with polar solvents. Considering our TA-spectroscopic experiments with suspended MOF crystallites, a significant scattering of the pump beam made it difficult to estimate the initial excited population as well as probe the TA signals for the triplets ($\lesssim$ 500 nm region). However, an upper limit for the triplet yields can be estimated. Given that SIU-150 has a total of ~10% radiative decay and ~85% of the residual population forms species $\mathbf{C}_{150}$, SIU-150 could potentially generate a maximum of 150% triplets (assuming no other non-radiative decay takes place) in MeTHF solvent. For SIU-152 and 175, the contribution from the delayed (TTA-repopulated) emission must be removed: which brings up a maximum possible triplet yield of 140% and 170%, respectively in MeTHF solvent. The SF can be facilitated in a polar solvent by modulating the mechanism by suppressing the S_{exc}-based route. Based on the extent of TTA-mediated delayed emission and other spectroscopic signatures, SIU-175 drives SF through a direct CT-based route and appears to be superior to the others. Given their solution stability and enormous opportunities (both structural and those achieved via various post-synthesis routes) relevant to energy and charge migration within such frameworks, such platforms can be exploited to harvest high-yield triplets in various energy-conversion schemes.

ASSOCIATED CONTENT

Supporting Information. Experimental details, computational and spectroscopic data. This material is available free of charge via the Internet at http://pubs.acs.org.

AUTHOR INFORMATION

Corresponding Author

* Pravas Deria

pderia@siu.edu.

ACKNOWLEDGMENT

P.D. gratefully acknowledges funding from the National Science Foundation (NSF CAREER CHE-1944903). D.A.G.-G. thanks for support from the NSF CAREER Award (CBET 1846707) and computational resources from the Colorado School of Mines (Mio Supercomputer). Work performed at the Center for Nanoscale Materials, a U.S. Department of Energy Office of Science User Facility, was supported by the U.S. DOE, Office of Basic Energy Sciences, under Contract No. DE-AC02-06CH11357. This research used Beamline 17-BM of the Advanced Photon Source; a U.S. Department of Energy (DOE) Office of Science User Facility operated for the DOE Office of Science by Argonne National Laboratory under Contract No. DE-AC02-06CH11357. JD and SG acknowledge the support from the U.S. Department of Energy, Office of Science, Office of Basic Energy Sciences via grant DE-FG02-87ER13808. Electron microscopic data were collected at EPIC facility, Northwestern University (supported by SHyNE Resource: NSF ECCS-2025633, the IIN, and NSF DMR-1720139). SSR thanks Doctoral Fellowship through the graduate school at SIU.

REFERENCES

(1) Smith, M. B.; Michl, J. Singlet Fission. *Chem. Rev.* **2010**, *110*, 6891-6936.
(2) Hanna, M.; Nozik, A. Solar conversion efficiency of photovoltaic and photoelectrolysis cells with carrier multiplication absorbers. *Int. J. Appl. Phys.* **2006**, *100*, 074510.
(3) Ullrich, T.; Munz, D.; Guldi, D. M. Unconventional singlet fission materials. *Chem. Soc. Rev.* **2021**, *50*, 3485-3518.
(4) Miller, C. E.; Wasielewski, M. R.; Schatz, G. C. Modeling Singlet Fission in Rylene and Diketopyrrolopyrrole Derivatives: The Role of the Charge Transfer State in Superexchange and Excimer Formation. *J. Phys. Chem. C* **2017**, *121*, 10345-10350.
(5) Berkelbach, T. C.; Hybertsen, M. S.; Reichman, D. R. Microscopic theory of singlet exciton fission. II. Application to pentacene dimers and the role of superexchange. *J. Chem. Phys.* **2013**, *138*, 114103.
(6) Pensack, R. D.; Tilley, A. J.; Grieco, C.; Purdum, G. E.; Ostroumov, E. E.; Granger, D. B.; Oblinsky, D. G.; Dean, J. C.; Doucette, G. S.; Asbury, J. B.; Loo, Y.-L.; Seferos, D. S.; Anthony, J. E.; Scholes, G. D. Striking the right balance of intermolecular coupling for high-efficiency singlet fission. *Chem. Sci.* **2018**, *9*, 6240-6259.
(7) Bae, Y. J.; Kang, G.; Malliakas, C. D.; Nelson, J. N.; Zhou, J.; Young, R. M.; Wu, Y.-L.; Van Duyne, R. P.; Schatz, G. C.; Wasielewski, M. R. Singlet Fission in 9,10-Bis(phenylethynyl)anthracene Thin Films. *J. Am. Chem. Soc.* **2018**, *140*, 15140-15144.
(8) Munson, K. T.; Gan, J.; Grieco, C.; Doucette, G. S.; Anthony, J. E.; Asbury, J. B. Ultrafast Triplet Pair Separation and Triplet Trapping following Singlet Fission in Amorphous Pentacene Films. *J. Phys. Chem. C* **2020**, *124*, 23567-23578.
(9) Zirzlmeier, J.; Lehnherr, D.; Coto, P. B.; Chernick, E. T.; Casillas, R.; Basel, B. S.; Thoss, M.; Tykwinski, R. R.; Guldi, D. M. Singlet fission in pentacene dimers. *Proc. Natl. Acad. Sci. U.S.A.* **2015**, *112*, 5325.
(10) Aster, A.; Zinna, F.; Rumble, C.; Lacour, J.; Vauthey, E. Singlet Fission in a Flexible Bichromophore with Structural and Dynamic Control. *J. Am. Chem. Soc.* **2021**, *143*, 2361-2371.
(11) Korovina, N. V.; Joy, J.; Feng, X.; Feltenberger, C.; Krylov, A. I.; Bradforth, S. E.; Thompson, M. E. Linker-Dependent Singlet Fission in Tetracene Dimers. *J. Am. Chem. Soc.* **2018**, *140*, 10179-10190.
(12) Wang, Z.; Liu, H.; Xie, X.; Zhang, C.; Wang, R.; Chen, L.; Xu, Y.; Ma, H.; Fang, W.; Yao, Y. Free-triplet generation with improved efficiency in tetracene oligomers through spatially separated triplet pair states. *Nat. Chem.* **2021**, *13*, 559-567.
(13) Kent, C. A.; Liu, D.; Ma, L.; Papanikolas, J. M.; Meyer, T. J.; Lin, W. Light Harvesting in Microscale Metal–Organic Frameworks by Energy Migration and Interfacial Electron Transfer Quenching. *J. Am. Chem. Soc.* **2011**, *133*, 12940-12943.
(14) Kent, C. A.; Mehl, B. P.; Ma, L.; Papanikolas, J. M.; Meyer, T. J.; Lin, W. Energy Transfer Dynamics in Metal–Organic Frameworks. *J. Am. Chem. Soc.* **2010**, *132*, 12767-12769.
(15) Maza, W. A.; Padilla, R.; Morris, A. J. Concentration Dependent Dimensionality of Resonance Energy Transfer in a Postsynthetically Doped Morphologically Homologous Analogue of UiO-67 MOF with a Ruthenium(II) Polypyridyl Complex. *J. Am. Chem. Soc.* **2015**, *137*, 8161-8168.
(16) Park, J.; Xu, M.; Li, F.; Zhou, H.-C. 3D Long-Range Triplet Migration in a Water-Stable Metal–Organic Framework for

Upconversion-Based Ultralow-Power in vivo Imaging. *J. Am. Chem. Soc.* **2018**, *140*, 5493-5499.
(17) Rowe, J. M.; Zhu, J.; Soderstrom, E. M.; Xu, W.; YakovenkoAndrey; Morris, A. J. Sensitized photon upconversion in anthracene-based zirconium metal–organic frameworks. *Chem. Commun.* **2018**, *54*, 7798-7801.
(18) Ha, D.-G.; Wan, R.; Kim, C. A.; Lin, T.-A.; Yang, L.; Voorhis, T. V.; Baldo, M. A.; Dincă, M. Exchange controlled triplet fusion in metal–organic frameworks. *Nature Mater.* **2022**, *21*, 1275-1281.
(19) Adams, M.; Kozlowska, M.; Baroni, N.; Oldenburg, M.; Ma, R.; Busko, D.; Turshatov, A.; Emandi, G.; Senge, M. O.; Haldar, R.; Wöll, C.; Nienhaus, G. U.; Richards, B. S.; Howard, I. A. Highly Efficient One-Dimensional Triplet Exciton Transport in a Palladium–Porphyrin-Based Surface-Anchored Metal–Organic Framework. *ACS Appl. Mater. Interfaces* **2019**, *11*, 15688-15697.
(20) Li, X.; Yu, J.; Gosztola, D. J.; Fry, H. C.; Deria, P. Wavelength-Dependent Energy and Charge Transfer in MOF: A Step towards Artificial Porous Light-Harvesting System. *J. Am. Chem. Soc.* **2019**, *141*, 16849-16857.
(21) Yu, J.; Park, J.; Van Wyk, A.; Rumbles, G.; Deria, P. Excited State Electronic Properties in Zr-based MOFs as a Function of Topological Network *J. Am. Chem. Soc.* **2018**, *140*, 10488-10496.
(22) Snellenburg, J. J.; Laptenok, S.; Seger, R.; Mullen, K. M.; van Stokkum, I. H. M. Glotaran: A Java-Based Graphical User Interface for the R Package TIMP. *J. Stat. Softw.* **2012**, *49*, 1 - 22.
(23) Anderson, R.; Gómez-Gualdrón, D. A. Increasing Topological Diversity During Computational "Synthesis" of Porous Crystals: How and Why. *CrystEngComm* **2019**, *21*, 1653-1665.
(24) Colón, Y. J.; Gómez-Gualdrón, D. A.; Snurr, R. Q. Topologically Guided, Automated Construction of Metal–Organic Frameworks and Their Evaluation for Energy-Related Applications. *Cryst. Growth Des.* **2017**, *17*, 5801-5810.
(25) Rappé, A. K.; Casewit, C. J.; Colwell, K. S.; Goddard, W. A. I.; Skiff, W. M. Uff, a Full Periodic Table Force Field for Molecular Mechanics and Molecular Dynamics Simulations. *J. Am. Chem. Soc.* **1992**, *114*, 10024-10035.
(26) Dassault Systèmes BIOVIA, Materials Studio, 6.0, San Diego: Dassault Systèmes, 2018
(27) Dubbeldam, D.; Calero, S.; Ellis, D. E.; Snurr, R. Q. RASPA: molecular simulation software for adsorption and diffusion in flexible nanoporous materials. *Mol. Simul.* **2016**, *42*, 81-101.
(28) With a low rotational energy barrier for anthracene moiety around the —C≡C— bond defining a degree of conjugation (see SI sec D1), computation of other torsional conformations where anthracene is rotated by 45° relative to the four carboxylates found to raise the E(T_1) to ca 1.22 eV –which still satisfy the energetic requirement for SF as the singlet energy is also being raised
(29) The corresponding computation models, however, were constructed without any solvent molecule present within the framework pores, which accounts for slight discrepancies in the intensity matching.
(30) Deria, P.; Gómez-Gualdrón, D. A.; Bury, W.; Schaef, H. T.; Wang, T. C.; Thallapally, P. K.; Sarjeant, A. A.; Snurr, R. Q.; Hupp, J. T.; Farha, O. K. Ultraporous, Water Stable, and Breathing Zirconium-Based Metal–Organic Frameworks with ftw Topology. *J. Am. Chem. Soc.* **2015**, *137*, 13183-13190.
(31) Yu, J.; Anderson, R.; Li, X.; Xu, W.; Goswami, S.; Surendran Rajasree, S.; Maindan, K.; Gómez-Gualdrón, D. A.; Deria, P. Improving Energy Transfer within Metal-Organic Frameworks by Aligning Linker Transition Dipole along Framework Axis. *J. Am. Chem. Soc.* **2020**, *142*, 11192-11202.
(32) The experimental values are usually higher compared to the PLATON 1.19 -predicted values (~80-94%; see SI sec C3) for the corresponding frozen crystallographic structures that do not consider anthracene flexibility.
(33) Samples were prepared by solvent exchange, not by solvent filling of a dried sample.
(34) Deria, P.; Yu, J.; Smith, T.; Balaraman, R. P. Ground-State versus Excited-State Interchromophoric Interaction: Topology Dependent Excimer Contribution in Metal–Organic Framework Photophysics. *J. Am. Chem. Soc.* **2017**, *139*, 5973-5983.
(35) Deria, P.; Yu, J.; Balaraman, R. P.; Mashni, J.; White, S. N. Topology-Dependent Emissive Properties of Zirconium-Based Porphyrin MOFs. *Chem. Commun.* **2016**, *52*, 13031-13034.
(36) Rajasree, S. S.; Yu, J.; Pratik, S. M.; Li, X.; Wang, R.; Kumbhar, A. S.; Goswami, S.; Cramer, C. J.; Deria, P. Superradiance and Directional Exciton Migration in Metal–Organic Frameworks. *J. Am. Chem. Soc.* **2022**, *144*, 1396-1406.
(37) Mitsui, M.; Kawano, Y.; Takahashi, R.; Fukui, H. Photophysics and photostability of 9,10-bis(phenylethynyl)anthracene revealed by single-molecule spectroscopy. *RSC Adv.* **2012**, *2*, 9921-9931.
(38) The excitation pump fluence (600 μJ/cm^2) used in these fs-TA experiments may cause singlet-singlet annihilation (SSA). However, the fs-TA dataset did not contain sufficient information to model such an ultrafast SSA process; see SI sec F2.
(39) Extended experiments with different MOF samples, including a pyrene-based NU-1000 suggest that this long-lived broad feature is not associated with triplets as it is not quenched by O2 or retinoic acid. Instead, it stems from, at least partly, two species: a low-energy complex and a singlet polar (/charge-transfer) excited state. The ns-TA experiment in polar solvents like DMF helped identify the SE from a low-energy trap state (possibly formed near any imperfect site and this excited state persists over several microseconds); their linewidth is sensitive to solvent dispersity. The origin of the CT state is currently under investigation. See SI sec I
(40) Deria, P.; Mondloch, J. E.; Tylianakis, E.; Ghosh, P.; Bury, W.; Snurr, R. Q.; Hupp, J. T.; Farha, O. K. Perfluoroalkane Functionalization of NU-1000 via Solvent-Assisted Ligand Incorporation: Synthesis and CO_2 Adsorption Studies. *J. Am. Chem. Soc.* **2013**, *135*, 16801-16804.
(41) Deria, P.; Bury, W.; Hupp, J. T.; Farha, O. K. Versatile Functionalization of the NU-1000 Platform by Solvent-Assisted Ligand Incorporation. *Chem. Commun.* **2014**, *50*, 1965-1968.
(42) Van Wyk, A.; Smith, T.; Park, J.; Deria, P. Charge-Transfer within Zr-Based Metal–Organic Frameworks: The Role of Polar Node. *J. Am. Chem. Soc.* **2018**, *140*, 2756-2760.
(43) Li, X.; Yu, J.; Lu, Z.; Duan, J.; Fry, H. C.; Gosztola, D. J.; Maindan, K.; Surendran Rajasree, S.; Deria, P. Photoinduced Charge Transfer with a Small Driving Force Facilitated by Exciplex-like Complex Formation in Metal–Organic Frameworks. *J. Am. Chem. Soc.* **2021**, *143*, 15286-15297.
(44) Berkelbach, T. C.; Hybertsen, M. S.; Reichman, D. R. Microscopic Theory of Singlet Exciton Fission. II. Application to Pentacene Dimers and the Role of Superexchange. *J. Chem. Phys.* **2013**, *138*, 114103.
(45) Schrauben, J. N.; Ryerson, J. L.; Michl, J.; Johnson, J. C. Mechanism of singlet fission in thin films of 1, 3-diphenylisobenzofuran. *J. Am. Chem. Soc.* **2014**, *136*, 7363-7373.
(46) Korovina, N. V.; Das, S.; Nett, Z.; Feng, X.; Joy, J.; Haiges, R.; Krylov, A. I.; Bradforth, S. E.; Thompson, M. E. Singlet fission in a covalently linked cofacial alkynyltetracene dimer. *J. Am. Chem. Soc.* **2016**, *138*, 617-627.
(47) Brown, K. E.; Salamant, W. A.; Shoer, L. E.; Young, R. M.; Wasielewski, M. R. Direct observation of ultrafast excimer formation in covalent perylenediimide dimers using near-infrared transient absorption spectroscopy. *J. Phys. Chem. Lett.* **2014**, *5*, 2588-2593.
(48) Mauck, C. M.; Hartnett, P. E.; Margulies, E. A.; Ma, L.; Miller, C. E.; Schatz, G. C.; Marks, T. J.; Wasielewski, M. R. Singlet

fission via an excimer-like intermediate in 3, 6-bis (thiophen-2-yl) diketopyrrolopyrrole derivatives. *J. Am. Chem. Soc.* **2016**, *138*, 11749-11761.
(49) This can be supported by a larger electronic coupling for the super-exchange process, which relatively scales by the extent of the respective LUMO energy-level perturbation compared to the HOMO-levels: See DFT computed energy on SIU-152 model in Figure S10.
(50) Islangulov, R. R.; Kozlov, D. V.; Castellano, F. N. Low Power Upconversion Using MLCT Sensitizers. *Chem. Commun.* **2005**, 3776-3778.
(51) Singh-Rachford, T. N.; Castellano, F. N. Triplet Sensitized Red-to-Blue Photon Upconversion. *J. Phys. Chem. Lett.* **2010**, *1*, 195-200.

TOC: